Delineating environmental control of phytoplankton biomass and phenology in the Southern Ocean

Mathieu Ardyna, Hervé Claustre, Jean-Baptiste Sallée, Francesco d'Ovidio, Bernard Gentili, Gert van Dijken, Fabrizio d'Ortenzio, Kevin Robert Arrigo

HAL Id: hal-01629465
https://hal.science/hal-01629465

Submitted on 15 Feb 2021

Delineating environmental control of phytoplankton biomass and phenology in the Southern Ocean

Authors: Mathieu Ardyna[1]*, Hervé Claustre[1], Jean-Baptiste Sallée[2], Francesco d'Ovidio[2], Bernard Gentili[1], Gert van Dijken[3], Fabrizio D'Ortenzio[1], Kevin Arrigo[3]

Affiliations:
[1]Sorbonne Universités, UPMC Univ Paris 06, INSU-CNRS, Laboratoire d'Océanographie de Villefranche, 181 Chemin du Lazaret, 06230 Villefranche-sur-mer, France

[2]Sorbonne Universités, UPMC Univ Paris 06, CNRS-IRD-MNHN, LOCEAN Laboratory, 4 Place Jussieu, Paris F-75005, France

[3]Department of Earth System Science, Stanford University, Stanford, California, USA

Main point #1: Phytoplankton phenology and biomass are mostly organized in the Southern Ocean at a large latitudinal scale and a regional scale.

Main point #2: The timing of bloom occurrence appears tightly linked to the seasonal cycle in irradiance, with some exceptions in specific light-limited regimes.

Main point #3: Zonal asymmetries in regional-scale phytoplankton biomass are mainly driven by local advective and iron supply processes.

Running head (40 characters max): Phytoplankton dynamics in the SO

Keywords: Phytoplankton ecology, Phytoplankton phenology, Biological pump, Climate Change, Southern Ocean, Remote sensing.

*Correspondence to: Mathieu.Ardyna@obs-vlfr.fr.

Abstract

The Southern Ocean (SO), an area highly sensitive to climate change, is currently experiencing rapid warming and freshening. Such drastic physical changes might significantly alter the SO's biological pump. For more accurate predictions of the possible evolution of this pump, a better understanding of the environmental factors controlling SO phytoplankton dynamics is needed. Here we present a satellite-based study deciphering the complex environmental control of phytoplankton biomass (PB) and phenology (PH; timing and magnitude of phytoplankton blooms) in the SO. We reveal that PH and PB are mostly organized in SO at two scales: a large latitudinal scale, and a regional scale. Latitudinally, a clear gradient in the timing of bloom occurrence appears tightly linked to the seasonal cycle in irradiance, with some exceptions in specific light-limited regimes (i.e. well-mixed areas). Superimposed on this latitudinal scale, zonal asymmetries, up to three orders of magnitude, in regional-scale PB are mainly driven by local advective and iron supply processes. These findings provide a global understanding of PB and PH in SO, which is of fundamental interest for identifying and explaining ongoing changes as well as predicting future changes in the SO biological pump.

1. Introduction

The Southern Ocean (SO) plays a key role in the global carbon cycle, absorbing 40% of the total oceanic inventory of anthropogenic CO_2 [*Khatiwala et al.*, 2009]. However, current and predicted changes in ocean circulation and hydrology associated with climate variability might impact the efficiency of the SO carbon sink, although the extent of such changes and their specific impact on the biological pump are still vigorously debated [*Landschützer et al.*, 2015; *Le Quéré et al.*, 2010; *Munro et al.*, 2015]. Such debate cannot advance without a better

69   understanding of the factors that shape the complex biogeography of the SO, and what controls

70   their time-scale of variability (i.e. daily, seasonal to decadal).

71   Delimiting marine bio-regions has proven highly valuable for disentangling multiple

72   limiting growth factors affecting the efficiency of the biological pump [*Longhurst*, 2007]

73   mediated by both PB and PH, and for ultimately underlining effects of climate change such as

74   areal changes in trophic regime [*Polovina et al.*, 2008] or in fisheries stock and species

75   [*Fossheim et al.*, 2015]. Changes in PB profoundly alter the efficiency of the biological pump,

76   thereby modulating energy transfer to upper trophic levels and carbon export to deep water

77   [*Legendre and Rassoulzadegan*, 1995]. Changes in PH may also have important consequences

78   for the marine food web, due to potential mismatch between primary and secondary producers

79   and apex predators [*Ardyna et al.*, 2014; *Edwards and Richardson*, 2004], and for the carbon

80   cycle through export of unexploited carbon aggregates to the deep ocean [*Dall'Olmo et al.*,

81   2016].

82   The efficiency of the SO's biological pump is strongly associated with phytoplankton

83   biomass (PB) and its phenology (PH), which themselves are mediated by nutrient availability

84   (e.g. mainly iron, and/or possibly nitrate and silicic acid), light, temperature and mortality factors

85   [*Behrenfeld and Boss*, 2014; *Boyd*, 2002]. These factors are essentially controlled by vertical

86   mixing, advection, seasonal fluctuations in solar irradiance, and the extent and typology of sea-

87   ice cover. As a result, a variety of patterns of net primary production (NPP) are found in the SO

88   [*Arrigo et al.*, 2008], with their own associated phytoplankton species succession, stock, and

89   distribution [*Quéguiner*, 2013]. Delineating the interplay of environmental forcing on PB and PH

90   remains challenging and requires novel approaches, which are available through satellite-derived

91   observations. Using these integrative and multidisciplinary approaches (i.e. satellite-derived

92 ocean color and altimetry, Argo floats, lagrangian modeling and biogeographic-derived

93 analysis), we provide here a global understanding of the phytoplankton biomass and phenology

94 in a potentially changing SO.

95 **2. Material and methods**

96 2.1 Satellite-derived, climatological and modeling products

97 Satellite-derived Level-3 data sets of chlorophyll-a concentration (chl a; mg m^{-3}) and

98 photosynthetically available radiation (PAR; E m^{-2} d^{-1}) were obtained from the European Space

99 Agency's GlobColour project (http://www.globcolour.info). Eight-day composite chl a

100 concentrations using standard Case 1 water algorithms were used (i.e. OC4v5 for SeaWIFS,

101 OC4Me for MERIS and OC3v5 for MODIS/VIIRS sensors; see *O'Reilly et al.* [2000] and

102 *Maritorena et al.* [2010] for details). The climatological annual net primary production (NPP)

103 was derived from the adapted-SO NPP model of *Arrigo et al.* [2008]. A detailed description of

104 the NPP model can be found in the supporting information [*Dobson and Smith*, 1988; *Gregg and*

105 *Carder*, 1990; *Markus*, 1999]. The climatologies of mixed layer depth and bathymetry were

106 extracted respectively from *Pellichero et al.* [2016] and the GEBCO, version 2014 (General

107 Bathymetric Chart of the Oceans; http://www.gebco.net). The climatology of the length of the

108 sea-ice cover was derived from the Special Sensor Microwave Imager (SSMI; 1998–2002) and

109 the Advanced Microwave Scanning Radiometer - Earth Observing System (AMSR-E; 2002–

110 2014) sensors, and made available by National Snow and Ice Data Center (NSIDC;

111 https://nsidc.org). The locations of the major fronts (i.e. the Subantarctic Front SAF, the

112 Antarctic Polar Front APF, the Southern Antarctic Circumpolar Current (ACC) Front SACCF

113 and the Southern Boundary of the ACC SBdy, following *Swart et al.* [2010]) were determined

114 based on the Maps of Absolute Dynamic Topography (MADT) product from CLS/AVISO. The

115 Lagrangian model of horizontal dispersion of iron fluxes used also altimeter products produced

116 by CLS/AVISO, with support from the CNES (Centre National d'Etudes Spatiales;

117 http://www.aviso.altimetry.fr/duacs/).

118   2.2. Clustering K-means method

119   The bio-regions were defined here using a cluster K-means analysis (see the SI for more

120 details), previously applied successfully in the Mediterranean Sea [*D'Ortenzio and Ribera*

121 *d'Alcalà*, 2009; *Mayot et al.*, 2016], in the North Atlantic [*Lacour et al.*, 2015] and at the global

122 scale [*D'Ortenzio et al.*, 2012]. The analysis was performed on climatological and normalized

123 annual chl *a* cycle, in order to statistically organize the GLOBcolour time series (1998–2014)

124 and to create clusters representing regions of similarity (i.e. annual chl *a* cycles). To maintain

125 consistency in the seasonal data availability throughout the study area, the period study covers

126 the period from September to March (as referred here to "annual"). This technique regroups

127 pixels with seasonal cycles shapes - i.e. similar phenologies. A single characteristic seasonal

128 cycle, that is statistically representative of the group as a whole, is then determined by

129 calculating the center (average cycle) within each group or cluster. Each group representative of

130 a characteristic seasonal cycle constitutes a phenological characteristic regime. A more detailed

131 discussion of the cluster K-means analysis can be found in the supporting information [*Devred et*

132 *al.*, 2007; *Hartigan and Wong*, 1979; *IOCCG*, 2009; *Lund and Li*, 2009; *Milligan and Cooper*,

133 1985]

134   A one-way analysis of variance by ranks (Kruskal–Wallis H test; *Zar* [2010]) was

135 performed to test whether eco-regions differed in their biological characteristics (i.e. annual

136 mean chlorophyll *a* concentration, seasonality and timing of bloom). A significant result of the

137 Kruskal–Wallis H test implies that at least one eco-region differs from all others.

138   2.3 Lagrangian modeling of horizontal iron fluxes

139   In order to estimate iron delivery due to horizontal stirring, we use an advection scheme

140   based on altimetry, extending to the Southern Ocean a Lagrangian model used for predicting the

141   development of the Kerguelen phytoplanktonic plume [*d'Ovidio et al.*, 2015]. The model has

142   been extensively calibrated and validated in the Crozet and Kerguelen regions by integrating

143   satellite data (altimetry and ocean color), lithogenic isotopes, iron measurements, and drifters

144   [*d'Ovidio et al.*, 2015; *Sanial et al.*, 2014; *Sanial et al.*, 2015]. The main characteristics of the

145   model were resumed here and we refer to *d'Ovidio et al.* [2015] for the full description of the

146   model. The model seeds each open ocean location with a particle and finds the particle's most

147   recent contact with a shallow bathymetry by a back-trajectory issued from altimetry data. It

148   provides the time and the position at which the contact took place. An exponential scavenging

149   relation (with a time constant based on in situ iron data from the KEOPS2 cruise) is used to

150   estimate the decreasing of bio-available iron along the trajectory from the time of the contact

151   with the potential iron source to the current position. Here, the model was applied to the entire

152   Southern Ocean using a grid of 0.25°, a time window of 2004-2015 (one map every 4 days),

153   potential sources of iron in the bathymetric band shallower than 500m, and a diffusion term of

154    $40 \text{ m}^2 \text{ s}^{-1}$.

155

156   **3. Results and discussion**

157   Based on satellite-derived observations, a large range of both annual mean chlorophyll *a*

158   (chl *a*) concentration and net primary production (NPP) (>0.1 mg chl *a* m^{-3}/20 g C $\text{m}^{-2} \text{ y}^{-1}$ to

159   more than 2 mg chl *a* m^{-3}/400 g C $\text{m}^{-2} \text{ y}^{-1}$, respectively) were observed across the SO. It occurs

160   at a variety of scales, including the latitudinal and the regional (i.e. Indian, Pacific and Atlantic;

161   Fig. 1a) scales in the SO. The annual mean chl *a* concentration is associated with the amplitude

162   of its seasonal cycle (Fig. 1a&c). In contrast, the timing of blooms (i.e. the maximum of the

163   annual chlorophyll cycles, Fig. 1d) appears entirely decoupled from both large-scale patterns in

164   annual chl *a* concentration and its seasonality (Fig. 1c), hence revealing a complex organization

165   of phenological patterns of the chl *a* annual cycle.

166   Here, we disentangle the spatial complexity of chl *a* seasonal cycle using a K-mean

167   clustering method [*D'Ortenzio et al.*, 2012] with the goal of defining distinct bio-regions with

168   similar large-scale patterns in PH (Fig. 2). In brief, this technique statistically gathers regions

169   that exhibit similarly shaped seasonal chl *a* cycles (see the section 2.2 for more details). The

170   seven distinct bio-regions so identified are distributed along a latitudinal gradient (Fig. 3a). At

171   temperate latitudes, two bio-regions (i.e. 1 and 2) exhibit an early bloom in October. Moving

172   south to 45-63°S, two other bio-regions (i.e. 4 and 5) display an annual chl *a* cycle with a

173   delayed bloom in November/December. Finally, near the Antarctic continental shelf (< 63°S),

174   the dominant bio-regions 6 & 7 were characterized by a late bloom in January/February.

175   Interestingly, one bio-region (i.e. 3) differs drastically from the general phenological trend of a

176   delayed bloom moving from subtropical to polar latitudes, having a late bloom at a moderate

177   latitude ($\approx 43°S$, Fig. 2 & 3d). Furthermore, the co-existence of bio-regions at a same latitude

178   indicates variations in the seasonality of the annual chl *a* cycle (e.g., 1 & 2, 4 & 5 and 6 & 7)

179   which are related to distinct levels of PB (Figs 3b-c).

180   From temperate to high latitudes, the latitudinal gradient in bloom timing clearly follows

181   changes in light regime (expressed as the annual mean photosynthetically available radiation in

182   the double boxplot; Fig. 4a). The unique bio-region (i.e., 3), characterized by a paradoxically late

183   bloom with respect to the timing of light availability, is mainly located in the vicinity of the

184   Antarctic Circumpolar Current. Interestingly, this region corresponds to the highest Southern

185   Ocean wind stress and depth of the mixed layer (see SI, Fig. S1). Deep mixed-layers likely

186   impose severe light limitation to phytoplankton growth in spring, hence delaying the bloom later

187   in season. Close to the Antarctic shelf, as shown locally in the western Antarctic Peninsula

188   [*Venables et al.*, 2013], the timing of the bloom (Fig. 2) was not related to winter sea-ice extent

189   but more to the seasonal cycle of irradiance.

190   To address the potential causes of regional-scale variability in PB (Fig. 1a), we hypothesize

191   that iron availability represents its first order driver [*Hutchins and Boyd*, 2016]. Using integrative

192   and multidisciplinary approaches, we disentangle the impact of four important iron supply

193   mechanisms on PB. These surface-layer iron-sources are shallow plateaus (<500 m) which both

194   (i) locally recharge the surface-layer in iron [*Arrigo et al.*, 2015; *Graham et al.*, 2015] and (ii)

195   remotely recharge the surface layer by lateral advection of non-consumed iron [*d'Ovidio et al.*,

196   2015; *Graham et al.*, 2015]; (iii) sea-ice, which recharges the surface as ice melts [*Arrigo et al.*,

197   2015; *Lannuzel et al.*, 2016]; and (iv) vertical mixing through deep convection, which can

198   entrain iron from deep water [*Tagliabue et al.*, 2014b]. Below, the potential impact of these four

199   likely iron-sources on the intensity of PB is investigated. Note that the Aeolian iron deposition

200   was not considered here as a major iron supply mechanism due to its intermittency and its

201   unclear role in regulating PB [*Boyd et al.*, 2012; *Cassar et al.*, 2007; *Tagliabue et al.*, 2009;

202   *Tagliabue et al.*, 2017].

203   Clearly, the highest PB (> 1.2 mg m^{-3}) are detected in shallow areas (< 500 m), on

204   continental and island shelves where iron fluxes are expected to be significant [*Boyd et al.*, 2012;

205   *Tagliabue et al.*, 2014a]. Furthermore, we use a Lagrangian model based on altimetry in order to

206   track which water parcels have been recently in contact with a shallow area – and when – to

207　　assess the probable locations of some of the iron plumes downstream of these iron sources and to

208　　estimate their loss of bio-available iron during advection by scavenging [*d'Ovidio et al.*, 2015].

209　　We find a well-defined decline in PB (from 0.8 to 0.3 mg m^{-3}) with distance and time from the

210　　most recent contact of the water parcel with a shallow area (Fig. 4b): the further away a water-

211　　parcel is from the initial shallow area iron source, or the longer after a water-parcel has been

212　　iron-enriched in shallow areas, the weaker is the PB signal. We note however that seamounts and

213　　submerged plateaus do not enhance local or downstream PB, as already observed north of

214　　Kerguelen plateau [*Graham et al.*, 2015] (Figs. 1a&4c), suggesting that not all shallow areas are

215　　active and/or bioavailable iron sources. Close to the Antarctic shelf and coastal polynyas, the

216　　potential role of the seasonal melting of sea-ice [*Arrigo et al.*, 2015; *Lannuzel et al.*, 2016] as

217　　iron source is revealed with enhanced PB ($\approx$0.4 mg m^{-3}).

218　　　　Moving away from potential iron delivery from shallow areas (either locally or

219　　downstream) and from sea-ice, we investigated the possible role of mixed-layer depth on

220　　regulating PB. If deepening of the mixed layer in winter can recharge the surface layer in

221　　nutrients (iron, but also nitrate and silicic acid in the temperate regimes) by deep convection, it

222　　can also limit PB by reducing light availability for phytoplankton growth during the growing

223　　season. Indeed, region of deep winter mixing in the Southern Ocean are mostly located directly

224　　north of the ACC, where strong winds and isopycnal tilts, are associated with an season-wide

225　　weak stratification, leading to deep winter mixed layer but also to relatively deep, compared to

226　　their surrounding, spring and summer mixed-layers.

227　　　　Our findings clearly translate this complex interplay between availability of nutrient and

228　　light related to the winter mixed-layer depth. An increase in PB is observed with the deepening

229　　of the winter mixed-layer until a maximum winter depth of about 150 m. When the winter mixed

230   layer becomes deeper, a decrease in PB is observed, likely resulting from a stronger light

231   limitation of phytoplankton growth during the growth season (Sep-Mar; on average, winter

232   mixed layer deeper than 150 m are associated to Sep-Mar mixed layer deeper than 110 m or so;

233   Fig 4b). We thus depict here a tipping winter MLD at ~ 150m, which likely represents a shift

234   between an iron-limited to a light-limited environment. Such threshold in the MLD is certainly

235   dependent on the local structure of the iron profile [*Tagliabue et al.*, 2014b]. Despite the HNLC

236   (High Nutrient Low Chlorophyll) nature of the Southern Ocean, an intermediate mixing mode

237   (i.e., with a winter MLD maximum from 120 to 200 meters) appears to enhance PB by supplying

238   an optimal combination of both light and nutrient requirements for phytoplankton growth. This

239   apparently modest effect of optimal mixing on PB may nevertheless have major implications due

240   to the large areal extension of those zones relying on the vertical mixing to support

241   phytoplankton iron requirements (Fig. 4c).

242   Deciphering the complexity of the SO's phytoplankton phenology and biomass is

243   particularly critical to assess how climate variability and change might regionally impact the

244   biological pump. Our results reveal two main scales of organization for both PB and PH, i.e. a

245   large latitudinal and a regional scale. Alterations of stratification that are expected with global

246   warming may modify light-mixing regimes, and thus potentially modulate the bloom timing.

247   However, since the phenology appears here to be strongly linked to the circumpolar seasonal

248   cycle in irradiance, we suppose that only drastic changes in stratification could significantly alter

249   bloom timing, and therefore the impact on the biological pump might be expected to be relatively

250   minor.

251   Concerning the fate of phytoplankton biomass in the changing SO, no particular changes at

252   local scale are expected in shallow bathymetry (i.e. where iron recharge from shallow plateaus

253   (<500 m) are not prone to be affected). Potential changes also likely to remain minor in

254   downstream transport from ACC, depending on whether the ACC has shifted locally in some

255   regions over the past decades according to climate model [*Kim and Orsi*, 2014; *Sallée et al.*,

256   2008] but not others [*Gille*, 2014; *Shao et al.*, 2015]. Even if ACC changes remain unclear under

257   next century climate change scenarios [*Meijers et al.*, 2012], past studies indicate that if there is a

258   change, the expected position change should be small compared to the size of the bathymetry

259   structure it interacts with to give rise to ocean surface iron plumes.

260   The main uncertainties regarding the fate of PB thus remains linked to the role of the

261   mixed-layer depth and the sea-ice, which have a more direct response to climate variability and

262   change. Climate modes have direct regional impact on both sea-ice and mixed-layer depth

263   [*Sallée et al.*, 2010; *Simpkins et al.*, 2012]. In response to SAM and ENSO, sea-ice extends in

264   some regions and is reduced in others, which, according to our results, would have regional

265   impact on iron delivery and PB intensity. Similarly, SAM tends to deepen mixed-layer depth

266   regionally but shallows it in other regions. Under next century climate change, the response is

267   more regionally consistent, with an overall shallowing of the mixed-layer associated with

268   increased stratification (freshwater input from glacier and sea-ice, and increased heat forcing

269   from the atmosphere), and an overall reduction of sea-ice cover.

270   However, according to our findings, a shallowing (or deepening) of the mixed-layer is not

271   expected to translate to the same PB response everywhere (see SI, Fig. S2). Indeed, the response

272   would be state-dependent: a shallowing of a deep mixed-layer (typically deeper than 200 m)

273   would result in an increase in PB, while a shallowing of an already relatively shallow mixed-

274   layer (typically less than 120 m), would reduce PB. At the SO scale, a global shallowing of the

275   mixed-layer depth appears to have negative consequences on PB (loss of ≈ 0.3 % m^{-1}; see SI),

276 mainly due to the areal increase of depleted-iron regions with less efficient vertical iron recharge.

277 Conversely, a positive response of PB (increase of ≈ 0.15 % m^{-1}; see SI) would be observed with

278 a global deepening of the mixed-layer until a critical threshold (+40 m compared to the actual

279 mixed-layer depth climatology), from which severe light limitation damps phytoplankton growth

280 and biomass. Given the more direct response of the MLD to climate variability and change in the

281 SO, these results highlight the crucial role of the local vertical mixing and the associated subtle

282 balance between light/nutrient availability on regulating PB in the majority of the HNLC areas of

283 the SO.

284

293

294 **Reference**

295 Ardyna, M., M. Babin, M. Gosselin, E. Devred, L. Rainville, and J.-É. Tremblay (2014), Recent
296 Arctic Ocean sea-ice loss triggers novel fall phytoplankton blooms, *Geophys. Res. Lett.*, *41*(17),
297 6207-6212.

298 Arrigo, K. R., G. L. van Dijken, and S. Bushinsky (2008), Primary production in the Southern
299 Ocean, 1997-2006, *J. Geophys. Res.*, *113*(C8), C08004.

300   Arrigo, K. R., G. L. van Dijken, and A. L. Strong (2015), Environmental controls of marine
301   productivity hot spots around Antarctica, *J. Geophys. Res.*, *120*(8), 5545-5565.

302   Behrenfeld, M., and E. Boss (2014), Resurrecting the Ecological Underpinnings of Ocean
303   Plankton Blooms, *Annu. Rev. Mar. Sci.*, *6*, 167-194.

304   Boyd, P. W. (2002), Environmental factors controlling phytoplankton processes in the Southern
305   Ocean, *J. Phycol.*, *38*(5), 844-861.

306   Boyd, P. W., K. R. Arrigo, R. Strzepek, and G. L. van Dijken (2012), Mapping phytoplankton
307   iron utilization: Insights into Southern Ocean supply mechanisms, *J. Geophys. Res.*, *117*(C6),
308   C06009.

309   Cassar, N., M. L. Bender, B. A. Barnett, S. Fan, W. J. Moxim, H. Levy, and B. Tilbrook (2007),
310   The Southern Ocean Biological Response to Aeolian Iron Deposition, *Science*, *317*(5841), 1067-
311   1070.

312   D'Ortenzio, F., and M. Ribera d'Alcalà (2009), On the trophic regimes of the Mediterranean Sea:
313   a satellite analysis, *Biogeosciences*, *6*(2), 139-148.

314   D'Ortenzio, F., D. Antoine, E. Martinez, and M. Ribera d'Alcalà (2012), Phenological changes of
315   oceanic phytoplankton in the 1980s and 2000s as revealed by remotely sensed ocean-color
316   observations, *Global Biogeochem. Cycles*, *26*(4), GB4003.

317   d'Ovidio, F., A. Della Penna, T. W. Trull, F. Nencioli, M. I. Pujol, M. H. Rio, Y. H. Park, C.
318   Cotté, M. Zhou, and S. Blain (2015), The biogeochemical structuring role of horizontal stirring:
319   Lagrangian perspectives on iron delivery downstream of the Kerguelen Plateau, *Biogeosciences*,
320   *12*(19), 5567-5581.

321   Dall'Olmo, G., J. Dingle, L. Polimene, R. J. W. Brewin, and H. Claustre (2016), Substantial
322   energy input to the mesopelagic ecosystem from the seasonal mixed-layer pump, *Nature Geosci*,
323   *9*(11), 820–823.

324   Devred, E., S. Sathyendranath, and T. Platt (2007), Delineation of ecological provinces using
325   ocean colour radiometry, *Mar. Ecol. Prog. Ser.*, *346*, 1-13.

326   Dobson, F. W., and S. D. Smith (1988), Bulk models of solar radiation at sea, *Q.J.R. Meteorol.*
327   *Soc.*, *114*(479), 165-182.

328   Edwards, M., and A. J. Richardson (2004), Impact of climate change on marine pelagic
329   phenology and trophic mismatch, *Nature*, *430*(7002), 881-884.

Fossheim, M., R. Primicerio, E. Johannesen, R. B. Ingvaldsen, M. M. Aschan, and A. V. Dolgov (2015), Recent warming leads to a rapid borealization of fish communities in the Arctic, *Nature Clim. Change*, *5*, 673–677.

Gille, S. T. (2014), Meridional displacement of the Antarctic Circumpolar Current, *Phil. Trans. R. Soc. A.*, *372*(2019), 20130273.

Graham, R. M., A. M. De Boer, E. van Sebille, K. E. Kohfeld, and C. Schlosser (2015), Inferring source regions and supply mechanisms of iron in the Southern Ocean from satellite chlorophyll data, *Deep Sea Research Part I: Oceanographic Research Papers*, *104*, 9-25.

Gregg, W. W., and K. L. Carder (1990), A simple spectral solar irradiance model for cloudless maritime atmospheres, *Limnol. Oceanogr.*, *35*(8), 1657-1675.

Hartigan, J. A., and M. A. Wong (1979), Algorithm AS 136: A K-Means Clustering Algorithm, *J. Roy. Stat. Soc. C-App.*, *28*(1), 100-108.

Hutchins, D. A., and P. W. Boyd (2016), Marine phytoplankton and the changing ocean iron cycle, *Nature Clim. Change*, *6*(12), 1072-1079.

IOCCG (2009), *Partition of the Ocean into Ecological Provinces: Role of Ocean-Colour Radiometry*, International Ocean Colour Coordinating Group, Dartmouth, Canada.

Khatiwala, S., F. Primeau, and T. Hall (2009), Reconstruction of the history of anthropogenic CO_2 concentrations in the ocean, *Nature*, *462*(7271), 346-349.

Kim, Y. S., and A. H. Orsi (2014), On the Variability of Antarctic Circumpolar Current Fronts Inferred from 1992–2011 Altimetry, *Journal of Physical Oceanography*, *44*(12), 3054-3071.

Lacour, L., H. Claustre, L. Prieur, and F. D'Ortenzio (2015), Phytoplankton biomass cycles in the North Atlantic subpolar gyre: a similar mechanism for two different blooms in the Labrador Sea, *Geophys. Res. Lett.*, 2015GL064540.

Landschützer, P., et al. (2015), The reinvigoration of the Southern Ocean carbon sink, *Science*, *349*(6253), 1221-1224.

Lannuzel, D., M. Vancoppenolle, P. v. d. Merwe, J. d. Jong, K. M. Meiners, M. Grotti, J. Nishioka, and V. Schoemann (2016), Iron in sea ice: Review and new insights, *Elem Sci Anth*, *4*, 000130.

Le Quéré, C., T. Takahashi, E. T. Buitenhuis, C. Rödenbeck, and S. C. Sutherland (2010), Impact of climate change and variability on the global oceanic sink of CO_2, *Global Biogeochemical Cycles*, *24*(4), GB4007.

361   Legendre, L., and F. Rassoulzadegan (1995), Plankton and nutrient dynamics in marine waters,
362   *Ophelia*, *41*, 153-172.

363   Longhurst, A. (2007), *Ecological Geography of the Sea (Second Edition)*, Academic Press,
364   Burlington.

365   Lund, R., and B. Li (2009), Revisiting Climate Region Definitions via Clustering, *J. Climate*,
366   *22*(7), 1787-1800.

367   Maritorena, S., O. H. F. d'Andon, A. Mangin, and D. A. Siegel (2010), Merged satellite ocean
368   color data products using a bio-optical model: Characteristics, benefits and issues, *Remote Sens.
369   Environ.*, *114*(8), 1791-1804.

370   Markus, T. (1999), Results from an ECMWF-SSM/I forced mixed layer model of the Southern
371   Ocean, *J. Geophys. Res.*, *104*(C7), 15603-15620.

372   Mayot, N., F. D'Ortenzio, M. Ribera d'Alcalà, H. Lavigne, and H. Claustre (2016), Interannual
373   variability of the Mediterranean trophic regimes from ocean color satellites, *Biogeosciences*,
374   *13*(6), 1901-1917.

375   Meijers, A. J. S., E. Shuckburgh, N. Bruneau, J.-B. Sallée, T. J. Bracegirdle, and Z. Wang
376   (2012), Representation of the Antarctic Circumpolar Current in the CMIP5 climate models and
377   future changes under warming scenarios, *J. Geophys. Res.*, *117*(C12), C12008.

378   Milligan, G., and M. Cooper (1985), An examination of procedures for determining the number
379   of clusters in a data set, *Psychometrika*, *50*(2), 159-179.

380   Munro, D. R., N. S. Lovenduski, T. Takahashi, B. B. Stephens, T. Newberger, and C. Sweeney
381   (2015), Recent evidence for a strengthening CO_2 sink in the Southern Ocean from carbonate
382   system measurements in the Drake Passage (2002–2015), *Geophys. Res. Lett.*, *42*(18),
383   2015GL065194.

384   O'Reilly, J., et al. (2000), SeaWiFS Postlaunch Calibration and Validation Analyses, Part 3*Rep.*,
385   NASA Goddard Space Flight Center.

386   Pellichero, V., J. B. Sallée, S. Schmidtko, F. Roquet, and J. B. Charrassin (2016), The ocean
387   mixed-layer under Southern Ocean sea-ice: seasonal cycle and forcing, *J. Geophys. Res. Oceans*.

388   Polovina, J. J., E. A. Howell, and M. Abecassis (2008), Ocean's least productive waters are
389   expanding, *Geophys. Res. Lett.*, *35*(3), L03618.

390   Quéguiner, B. (2013), Iron fertilization and the structure of planktonic communities in high
391   nutrient regions of the Southern Ocean, *Deep Sea Res. Pt. 2*, *90*(0), 43-54.

392 Sallée, J. B., K. Speer, and R. Morrow (2008), Southern Ocean fronts and their variability to
393 climate modes, *J. Climate*, *21*(12), 3020-3039.

394 Sallée, J. B., K. G. Speer, and S. R. Rintoul (2010), Zonally asymmetric response of the Southern
395 Ocean mixed-layer depth to the Southern Annular Mode, *Nature Geosci*, *3*(4), 273-279.

396 Sanial, V., P. van Beek, B. Lansard, F. d'Ovidio, E. Kestenare, M. Souhaut, M. Zhou, and S.
397 Blain (2014), Study of the phytoplankton plume dynamics off the Crozet Islands (Southern
398 Ocean): A geochemical-physical coupled approach, *J. Geophys. Res. Oceans*, *119*(4), 2227-
399 2237.

400 Sanial, V., P. van Beek, B. Lansard, M. Souhaut, E. Kestenare, F. d'Ovidio, M. Zhou, and S.
401 Blain (2015), Use of Ra isotopes to deduce rapid transfer of sediment-derived inputs off
402 Kerguelen, *Biogeosciences*, *12*(5), 1415-1430.

403 Shao, A. E., S. T. Gille, S. Mecking, and L. Thompson (2015), Properties of the Subantarctic
404 Front and Polar Front from the skewness of sea level anomaly, *J. Geophys. Res.*, *120*(7), 5179-
405 5193.

406 Simpkins, G. R., L. M. Ciasto, D. W. J. Thompson, and M. H. England (2012), Seasonal
407 Relationships between Large-Scale Climate Variability and Antarctic Sea Ice Concentration, *J.*
408 *Climate*, *25*(16), 5451-5469.

409 Swart, S., S. Speich, I. J. Ansorge, and J. R. E. Lutjeharms (2010), An altimetry-based gravest
410 empirical mode south of Africa: 1. Development and validation, *J. Geophys. Res.*, *115*(C03002),
411 2156-2202.

412 Tagliabue, A., L. Bopp, and O. Aumont (2009), Evaluating the importance of atmospheric and
413 sedimentary iron sources to Southern Ocean biogeochemistry, *Geophys. Res. Lett.*, *36*(13),
414 L13601.

415 Tagliabue, A., O. Aumont, and L. Bopp (2014a), The impact of different external sources of iron
416 on the global carbon cycle, *Geophys. Res. Lett.*, *41*(3), 920–926.

417 Tagliabue, A., J.-B. Sallée, A. R. Bowie, M. Levy, S. Swart, and P. W. Boyd (2014b), Surface-
418 water iron supplies in the Southern Ocean sustained by deep winter mixing, *Nature Geosci*, *7*(4),
419 314-320.

420 Tagliabue, A., A. R. Bowie, P. W. Boyd, K. N. Buck, K. S. Johnson, and M. A. Saito (2017),
421 The integral role of iron in ocean biogeochemistry, *Nature*, *543*(7643), 51-59.

422   Venables, H. J., A. Clarke, and M. P. Meredith (2013), Wintertime controls on summer
423   stratification and productivity at the western Antarctic Peninsula, *Limnol. Oceanogr.*, *58*(3),
424   1035–1047.

425   Zar, J. (2010), *Biostatistical Analysis, 5th edition*, Pearson Prentice Hall, New Jersey.
426

Figure captions

428

429 <u>**Figure 1:**</u> **Phytoplankton biomass, net primary production and phenology in the Southern**

430 **Ocean.** Map showing the climatological (a) annual mean chlorophyll *a* concentration (mg m^{-3}),

431 (b) annual net primary production (g C m^{-2} d^{-1}), (c) the chlorophyll *a* seasonality (mg m^{-3}), (d)

432 the timing of the bloom (week) maximum based on the GLOBcolour time series (1998–2014).

433 The climatological annual net primary production (b; mg C m^{-2} d^{-1}) was derived from the

434 adapted-SO NPP model of Arrigo et al. (2008). Frontal positions calculated from MADT

435 contours are shown for the STF (white), the SAF (red), the PF (yellow) and the SACCF (black).

436

437 <u>**Figure 2:**</u> **Biogeography of the Southern Ocean.** Spatial distribution (a) of the 7 bio-regions

438 (i.e. bio-regions 1 to 7) of the Southern Ocean obtained from the k-means analysis. The

439 normalized annual chlorophyll cycles (continuous lines) of the centers of the clusters (b − h)

440 obtained from the k-means analysis are presented, as well as their respective standard deviation.

441 The absolute annual chlorophyll cycles (dashed lines) corresponding to the centers of the clusters

442 (b − h) are also indicated.

443

444 <u>**Figure 3:**</u> **Latitudinal repartition of the bio-regions and their respective biological**

445 **characteristics.** Latitudinal proportion (a) of the different bio-regions. Box plots of the bio-

446 regions (1 to 7; x axis) against (b) annual mean chlorophyll *a* concentration (mg m^{-3}), (c) the

447 chlorophyll a seasonality (mg m^{-3}), (d) the timing of the bloom maximum (month; y axis). The

448 line in the middle of each box represents the region median. The top and bottom limits of each

449 box are the 25th and 75th percentiles, respectively. The lines extending above and below each

450   box, i.e., whiskers, represent the full range of non-outlier observations for each variable beyond

451   the quartile range. The results of the Kruskal–Wallis H test are shown in figures (b) through (d),

452   and depict regions with statistically significant differences between the climatological input

453   variables at the 95 % level ($p < 0.05$). The codes of the test significance are as follow .: $p < 0.05$,

454   *: $p < 0.01$, **: $p < 0.001$ and ***: $p < 0.0001$.

455

456   **Figure 4: Environmental control of phytoplankton biomass and phenology in the Southern**

457   **Ocean.** Double boxplot (a) of the maximum bloom timing (weeks) versus the annual mean PAR

458   (E m y^{-1}) of the different bio-regions. The top/right and bottom/left limits of each box are the

459   25th and 75th percentiles, respectively. The numbers in each box are located at the median of

460   both maximum bloom timing and annual mean PAR. Barplot (b) of the mean annual

461   chlorophyll *a* concentration according (1) the shallow areas (< 500 m; red), (2) areas where iron

462   delivery downstream take place (%; percent of iron remaining in a water parcel after scavenging

463   in respect to its initial concentration acquired in shallow areas; red to blue), (3) areas

464   characterized by a seasonal sea-ice cover (grey) and (4) areas where variations in the annual

465   maximum MLD are analyzed (white). See the map (c) delineating the distinct areas listed just

466   above.

467

Figure 1.
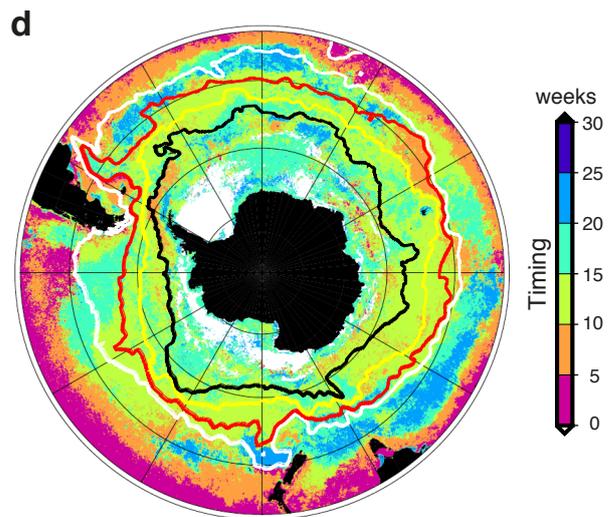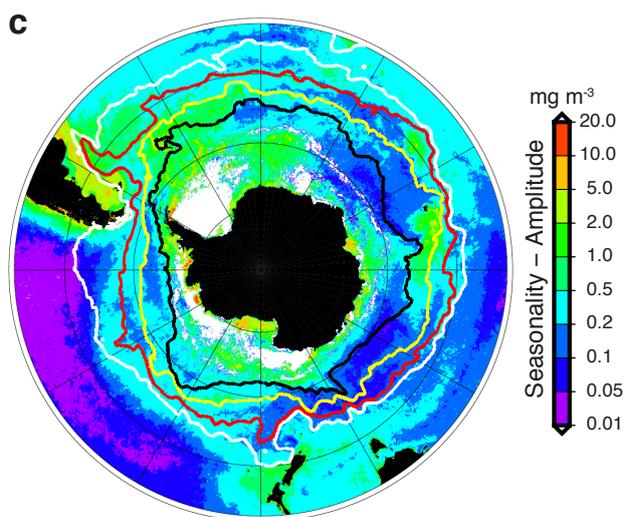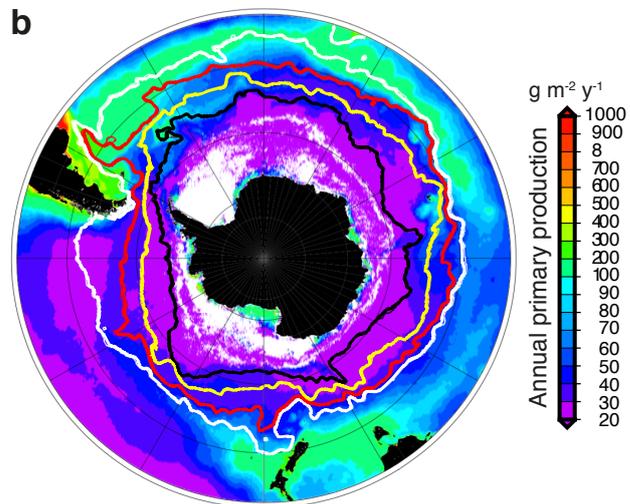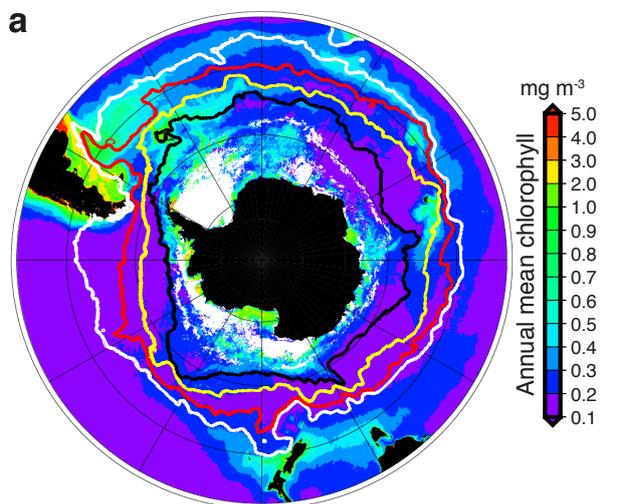
Figure 2.

a
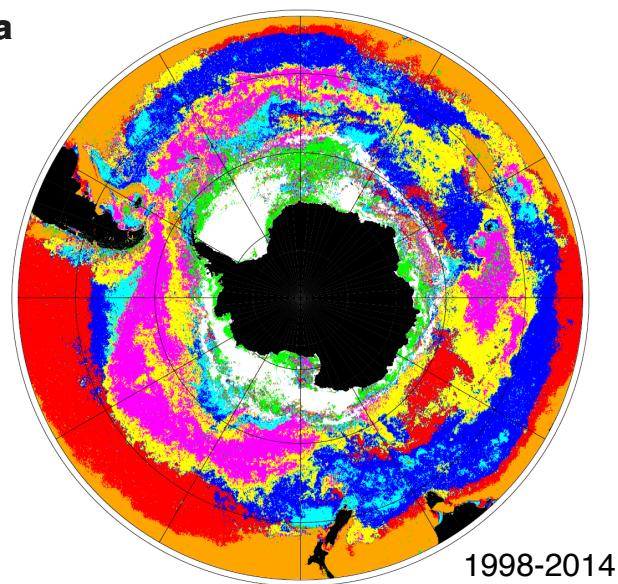
Index

Bio-region

7
6
5
4
3
2
1

1998-2014

b Clust. 1 10 %

c Clust. 2 15 %

d Clust. 3 18 %

e Clust. 4 20 %

f Clust. 5 17 %

g Clust. 6 10 %

h Clust. 7 10 %

Normalized chlorophyll *a*
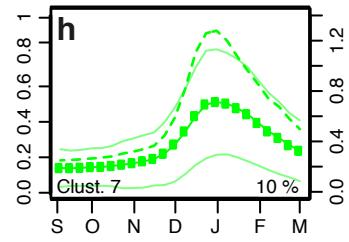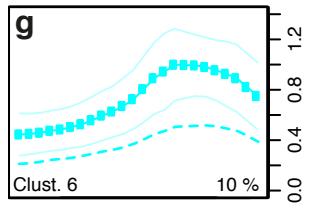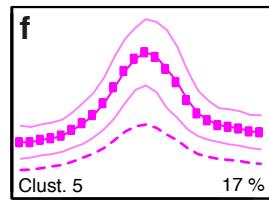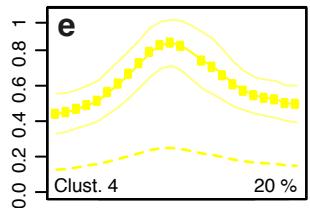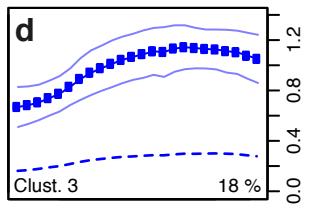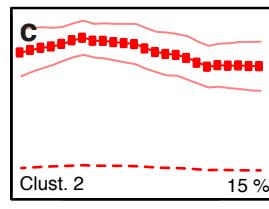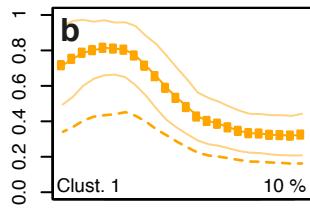
Absolute chlorophyll *a* (mg m^{-3})

Month

S O N D J F M

Figure 3.

Figure 4.

a (top axis) 7 6 5 4 3 2 1

Bloom timing (month): F J D N O S

Mean annual PAR (E m^{-2} d^{-1}): 10 20 30 40 50

(right axis) 7 3 / 4 5 / 2 1

b Mean annual chlorophyll a (mg m^{-3})

Horizontal stirring: Iron delivery | Sea-Ice period | Annual MLD maximum

Bathymetry (>500m)
>75 %
50 % - 75 %
20 % - 50 %
10 % - 20 %
5 % - 10 %
1 % - 5 %
0.5 % - 1 %
0.2 % - 0.5 %
0.1 % - 0.2 %
0.05 % - 0.1 %
> 150 d
100 -150 d
50 -100 d
20 - 50 d
1 - 20 d
0 m - 100 m
100 m - 125 m
125 m - 150 m
150 m - 200 m
200 m - 250 m
250 m - 300 m
>300 m

Mean MLD (from Sept. to Mar.)
40 m 60 m 80 m 100 m 120 m 140 m 160 m 180 m

c

%
100
75
50
20
10
5
2
1
0.5
0.2
0.1
0.05

Iron delivery

Sea-ice period
day
0
20
50
100
150
200
250